Advances in Science, Technology and Engineering Systems Journal
Vol. 11, No. 4, 35-45 (2026)
www.astesj.com
Special Issue on Emerging Multidisciplinary Directions in Engineering, Computing, and Applied Sciences

ASTESJ
ISSN: 2415-6698

Machine Learning-Based Crop Growth Diagnosis System Using Spatiotemporal Relative Analysis of Vegetation Indices via a Quartile-Based Method

Taichi Ito*, Ken'ichi Minamino

Graduate School of Software and Information Science, Iwate Prefectural University, Takizawa, 0200693, Japan

Email(s): s236w001@s.iwate-pu.ac.jp (T. Ito), minamino@iwate-pu.ac.jp (K. Minamino)

*Corresponding Author: Taichi Ito, Iwate Prefectural University, Takizawa, Japan, Email: taichi12820@gmail..com

A R T I C L E I N F O

Article history:
Received: 21 July, 2026
Revised: 18 August, 2026
Accepted: 22 August, 2026
Online: 30 August, 2026

Keywords:
Geographic Information System
Machine Learning
Paddy Rice
Remote Sensing
Smart Agriculture
Unmanned Aerial Vehicle

A B S T R A C T

Japanese agriculture faces pressing challenges, including a declining and aging farming population and the need to adapt to climate change. To address these issues, Smart Agriculture is being introduced to improve production efficiency. Among these, unmanned aerial vehicles (UAVs) have gained attention for their ability to rapidly monitor entire fields. We proposed a machine learning-based crop growth diagnosis system that generates spatiotemporal data for multiple vegetation indices (VIs) using the quartile method and diagnoses crop growth based on patterns of change in these values. The experimental site consisted of five paddy fields within an 80 m × 50 m plot in Iwate Prefecture, Japan, equipped with weather and water sensors. Ground-truth data (overall length, culm length, panicle number, and stem number) were collected approximately one week before harvest. UAV monitoring was conducted four times using a multispectral camera, and growth analysis was performed with six VIs. Correlation analysis revealed a positive relationship between crop growth and the daily average water level during the drainage period, and a negative relationship with the daily temperature range in mid-June. A combined cluster-label representation, constructed from clustering results of all VIs for each mesh, enabled integrated analysis and visualization of multi-index patterns. Grid size optimization showed no significant differences in correlation trends between 1 m × 1 m and 5 m × 5 m resolutions. For non-crop area removal, a comparison of three image segmentation methods demonstrated that the Otsu Method achieved the highest performance. Finally, to facilitate practical use in the field, we prototyped a report interface for the diagnosis system. Future work will focus on developing a comprehensive field diagnosis system to clarify field environments, with the aim of addressing fragmentation and enclaves in Japanese farms.

1. Introduction

Japanese agriculture is currently facing two major challenges. The first is the declining and aging farmer population. Government statistics report that the farming population in 2025 was 1.036 million, representing a decrease of approximately 300,000 people every five years. Furthermore, 69.6% of farmers are aged 65 years or older, and the sector continues to struggle with a shortage of successors [1]. The second challenge is adaptation to climate change. According to the government's Climate Change Monitoring, the years 2023–2025 recorded the highest annual global surface temperatures since 1891 [2]. In particular, 2023 marked the first year in which high temperatures directly affected crop production in Japan. For rice cultivation, the proportion of rice rated as top grade in appearance fell sharply from 78.6% in 2022 to 60.9% in 2023 [3], [4]. Elevated temperatures accelerated growth by more than a week compared with normal years, leaving farmers unable to keep pace with fieldwork. These unstable production conditions also contributed to rising rice prices. Given these circumstances, there are growing expectations for the adoption of smart agriculture technologies to improve production efficiency, strengthen crop management, and formalize agricultural practices.

Numerous studies have been conducted in this field. In [5], the authors proposed a model that simultaneously accounts for temporal and vertical (spatial) variations in soil moisture using ground-based sensors and machine learning. However, this approach requires considerable effort for installation and cannot easily assess crop growth across entire fields. The agricultural use of unmanned aerial vehicles (UAVs) has attracted attention as a means of monitoring crop growth at scale [6]. For example, in [7], the authors employed UAV multispectral imagery and machine learning in corn fields to evaluate spatiotemporal yield variability based on the relationship between growth stages and yield. However, yield prediction remains highly dependent on crop species and region, and this study did not evaluate temporal changes in crop growth status. In [8], the authors reported a framework that used deep learning to extract changes in time-series data from UAV images. However, these approaches primarily focus on large-scale change detection, such as cropping conditions and crop species distributions. As described above, research on the utilization of spatiotemporal data in smart agriculture has largely concentrated on sensor-based prediction models, which require significant field labor and costs; yield prediction models that struggle to account for variations across crop species and regions; and macro-level change detection, such as regional land use and cropping conditions. In contrast, few studies have focused on continuous changes in crop growth conditions and spatial heterogeneity within individual fields.

This study analyzed and visualized remote sensing data to support the development of a farm field diagnostic system using UAV multispectral imagery. UAV survey data are typically acquired from aerial photographs, requiring photogrammetry and geographic information systems (GIS) software for analysis. However, the limited availability of manuals for such software makes the process challenging. To address this issue, we build on a previous study [9] that developed a Python-based analysis workflow automation, enabling visualization of crop growth conditions. By integrating and analyzing these visualization results, we discuss the usefulness of a farm diagnostic system. The remainder of this paper is organized as follows: Section 2 describes the proposed system and processing workflow, experimental site and hardware used, construction of a spatiotemporal dataset from UAV multispectral imagery, and methods applied to time-series data analysis. Section 3 presents the results of spatiotemporal analysis and visualization. Section 4 discusses the optimization of the analysis process, including the effects of mesh size on the correlation analysis, methods for removing non-crop areas during the early growth stage, and automation of QGIS-based workflows using Python. Finally, Section 5 summarizes the findings and discusses future applications.

2. Materials and Methods

2.1. Proposed Crop Growth Diagnosis System

This paper proposes a machine learning-based crop growth diagnosis system that utilizes UAV-acquired multispectral imagery. The system automatically generates spatiotemporal datasets of multiple vegetation indices (VIs) and analyzes crop growth by integrating three complementary approaches: quartile-based analysis, clustering-based analysis, and GIS visualization. The effectiveness of the proposed system was evaluated through experiments conducted in a paddy field.

Figure 1 illustrates the workflow of the proposed crop-growth diagnosis system. The proposed system comprises survey planning, UAV image acquisition, image preprocessing, grid-size optimization, data preprocessing, and spatiotemporal analysis (machine learning and GIS-based visualization). Each module was designed to generate diagnostic information from UAV-acquired multispectral imagery. Survey planning is the first step in the proposed system. UAV surveys should be conducted at appropriate growth stages depending on the monitoring target. Typically, surveys are performed during major growth stages to efficiently capture temporal changes while reducing labor

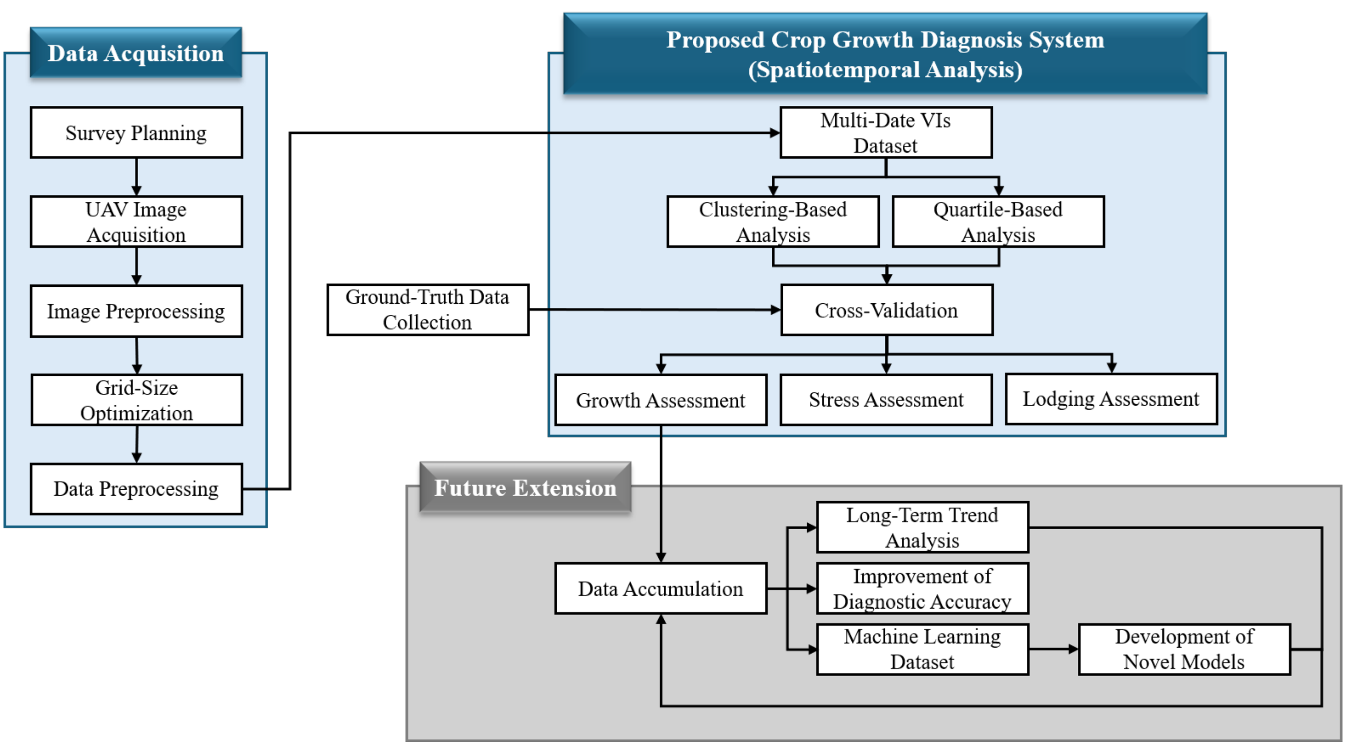

Figure 1: Workflow of Spatiotemporal Analysis Using UAV-Based Multispectral Images

requirements [10]. However, adverse weather may require flight surveys to be rescheduled, potentially introducing image noise and causing UAV malfunctions. Rescheduled surveys should still coincide with critical crop growth stages. After the UAV image acquisition, the proposed system performs image preprocessing, including reflectance calibration, grid-size optimization, and mesh generation to construct spatiotemporal datasets for machine learning. Because reflectance values are affected by weather conditions and imaging times [11], crop growth must be evaluated using time-series data rather than relying solely on single-date imagery. To solve this problem, the proposed system produces time-series VI datasets for each mesh and applies unsupervised learning to reduce the dependence on specific regions and crop species. The proposed system assesses crop growth from two complementary perspectives: quartile-based analysis captures relative spatial variability while reducing outlier effects, whereas clustering-based analysis characterizes temporal changes in VI values based on their temporal patterns. These results are then integrated for comprehensive pattern analysis. In addition, the system includes grid-size optimization and image calibration under low-vegetation cover conditions to improve the analysis accuracy. By integrating multiple VI analyses with GIS visualization, the proposed system provides a comprehensive assessment of crop growth. The proposed system can be applied regardless of the crop species or region, even during the first year of data collection. Furthermore, the accumulation of multiyear data from the same field is expected to facilitate the analysis of long-term change analysis and improve diagnostic accuracy.

2.2. Experimental Site and Hardware

Figure 2 shows the location and aerial images of the experimental site. The site is an approximately 80 m × 50 m plot located in Iwate Prefecture, Japan, consisting of five paddy fields (Fields A to E) arranged from north to south. The site is bordered by a road to the north, a farm road to the east, paddy fields to the south, and a waterway to the west. The edible rice variety Ginga-no-Shizuku was planted in all paddy fields on May 23, 2025, and harvested on September 22, 2025. Prior to planting, a basal fertilizer containing nitrogen, phosphorus, and potassium (15% each) was applied on May 1 at a rate of 40 g/m². No additional fertilizer was applied during the cultivation period.

Figure 3 shows the hardware components of the proposed crop-growth diagnosis system. A multispectral UAV equipped with visible light (RGB) and four spectral bands (560, 650, 730, and 860 nm, corresponding to Green, Red, Red-Edge, and NIR, respectively) was used for aerial observations. For image calibration, a gray standard reflector GK-1 (CHUO PRECISION INDUSTRIAL CO., LTD., Japan) was utilized. In addition, a weather sensor was installed in Field B. This sensor can record seven parameters (namely, temperature, humidity, light intensity, precipitation, wind speed, wind direction, and atmospheric pressure) at 5-min intervals. Four water sensors were installed in Fields C and D, each recording water temperature and water level at 15-min intervals. Image processing and visualization were conducted using the photogrammetry software Agisoft Metashape Professional 2.2 (Agisoft LLC, Russia), and the geographic information system software QGIS 3.44.

2.3. Data Collection

Aerial photographs were acquired on June 25, July 25, August 21, and September 19, 2025. The UAV was flown at an altitude of 40 m above ground level, yielding a spatial resolution of approximately 2–3 cm/pixel. The front overlap and sidelap rates were set to 80% and 70%, respectively. Under these flight parameters, each survey was completed within approximately 3 min. Immediately after each flight, both sides of the GK-1 reflector were photographed manually to enable reflectance calibration. Orthomosaic images were generated using Agisoft Metashape Professional and subsequently imported into QGIS for visualization and analysis. To evaluate the proposed system, ground-truth data were collected on September 16, 2025. Ten rice plants were sampled from the second row from field edges near

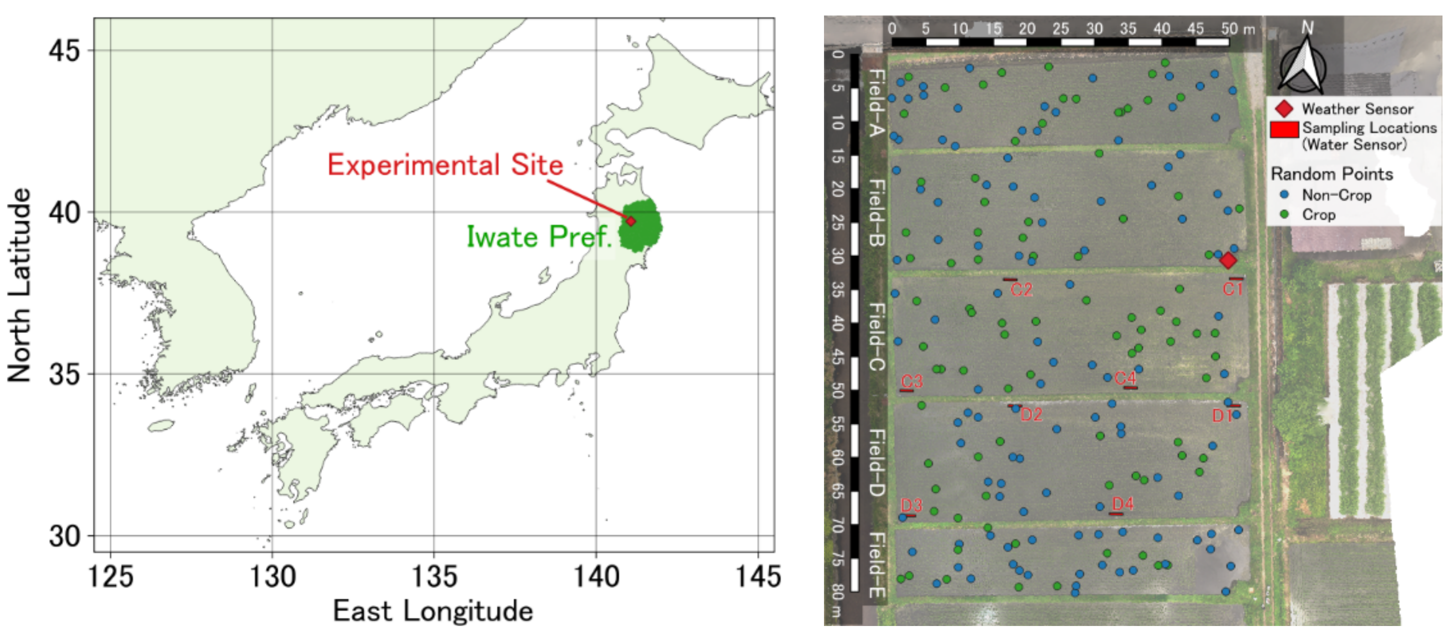

Figure 2: Location and Aerial Image of The Experimental Site

Table 1: Vegetation Indices Used

Index		Equation	Ref.
Green-type • photosynthetic activity • chlorophyll	GNDVI	$\frac{\mathrm{NIR}-\mathrm{Green}}{\mathrm{NIR}+\mathrm{Green}}$	[12]
	$\mathrm{CI_{Green}}$	$\frac{\mathrm{NIR}}{\mathrm{Green}}-1$	[13]
Red-type • vegetation • health	NDVI	$\frac{\mathrm{NIR}-\mathrm{Red}}{\mathrm{NIR}+\mathrm{Red}}$	[14]
	RVI	$\frac{\mathrm{NIR}}{\mathrm{Red}}$	[15]
Red-Edge-type • non-stress level • health (late growth stage)	NDRE	$\frac{\mathrm{NIR}-\mathrm{RedEdge}}{\mathrm{NIR}+\mathrm{RedEdge}}$	[16]
	$\mathrm{CI_{RedEdge}}$	$\frac{\mathrm{NIR}}{\mathrm{RedEdge}}-1$	[17]

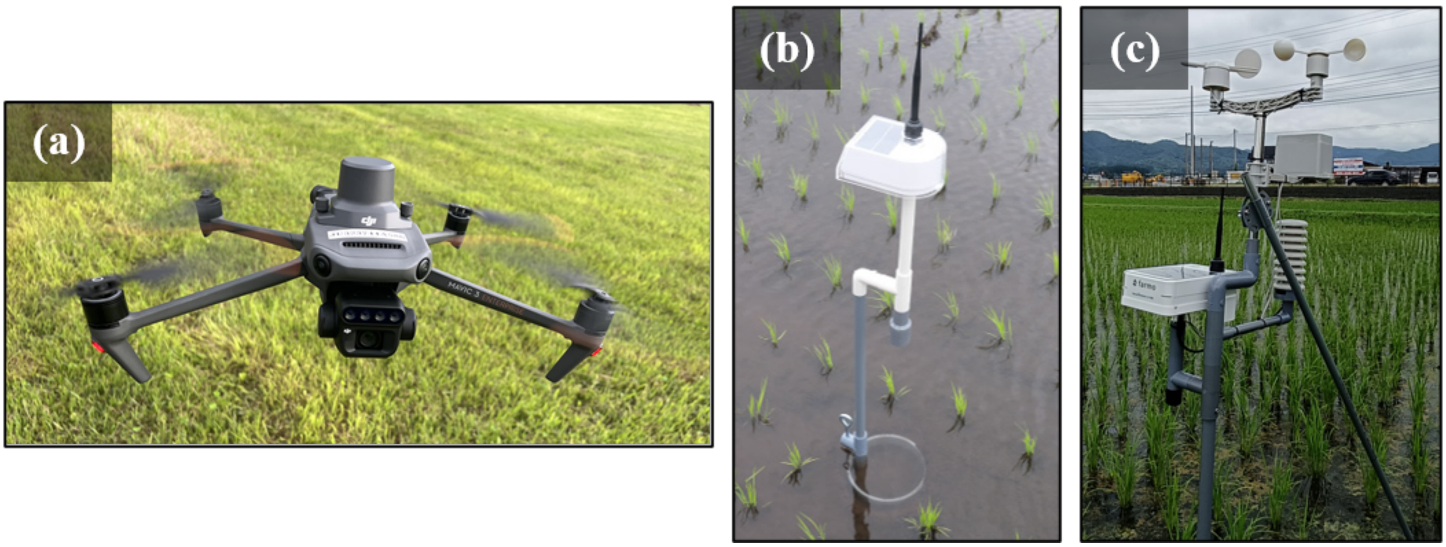

Figure 3: Equipment Used.
(a) UAV (Mavic 3M, DJI Co., Ltd., China), (b) Water Temperature/Depth Sensor (farmo Co., Ltd., Japan), and (c) Weather Sensor (farmo Co., Ltd., Japan).

each water sensor. The following five parameters were measured: overall length, culm length, panicle number, stem number, and lodging degree. However, the limited sample size necessitates further data collection and statistical validation.

2.4. Analytical Approach in This Study

VIs are widely used to quantify the crop growth conditions based on the spectral reflectance characteristics of plants and soil [18]. Numerous VIs have been developed to estimate vegetation status, nitrogen content, biomass, and other crop characteristics by exploiting differences or ratios between spectral bands [19], [20]. The proposed system utilizes the six VIs listed in Table 1, consistent with those employed in previous studies [9], [10], [21]. Each VI combines the near-infrared (NIR) band with another spectral band, and the indices are categorized accordingly. The diagnostic parameters for each VI type are similar: the green type assesses photosynthetic activity and chlorophyll content, the red type assesses vegetation vigor and overall plant health, and the red-edge type captures non-stress levels and crop health during late growth stages. For spatiotemporal analysis, the experimental fields were virtually divided into mesh grids of several meters, and time-series VI datasets were generated for each mesh [10], [21]. A correlation analysis was first conducted between VI values and ground-truth data. Quartile-based analysis assessed relative spatial variability at each survey date, while clustering-based analysis using TimeSeriesKMeans with the Euclidean distance metric [22] characterized temporal changes in VI values and classified experimental sites by growth trends. After clustering each VI time series, the results were further analyzed by combining cluster IDs across all VIs. As demonstrated in [9], this integrated cluster-label representation enabled visualization of complex growth patterns, such as lodging and water stress, which could not be identified through clustering of individual VIs alone.

3. Results

3.1. Comparison with Ground-Truth Data

Figure 4 presents bar charts of the mean and standard deviation for the ten plants collected at each sampling point, corresponding to the “Sampling Locations” in Figure 2. Lodging degree was rated on a six-point scale (0 = none, 5 = complete lodging). Because 13 of the 80 plants were rated as Level 1 and the remainder as Level 0, the site was considered to have no lodging. Sample point C2

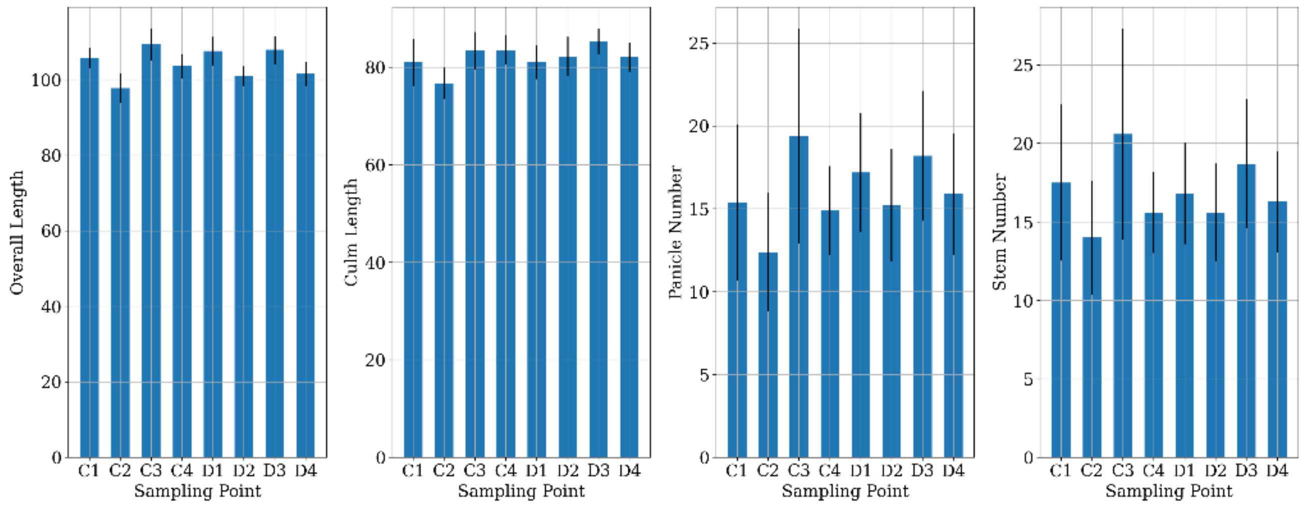

Figure 4: Bar chart of Sampling Survey Items

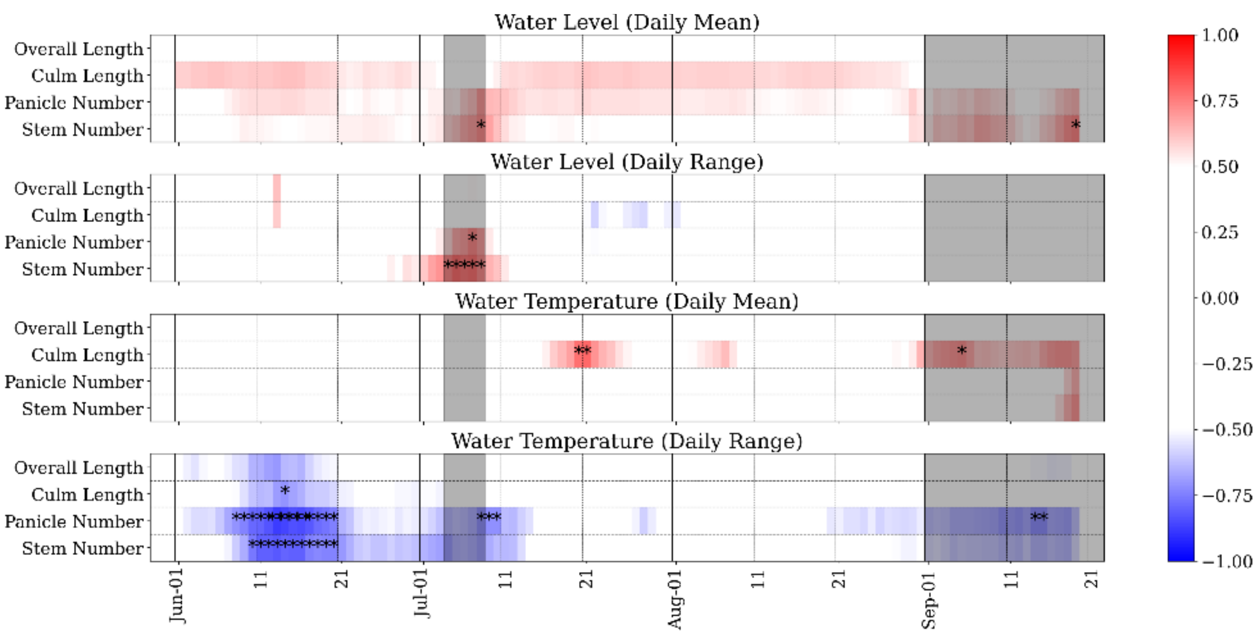

Figure 5: Correlations between Water Sensor Data and Survey Items. *: significant at the 5% level. The drainage period is highlighted in gray.

consistently exhibited lower values across all parameters. One-way analysis of variance (ANOVA) revealed statistically significant differences in the means across sampling points for four parameters: overall length ($p = 3.906 \times 10^{-11}$), culm length ($p = 1.022 \times 10^{-4}$), panicle number ($p = 1.403 \times 10^{-2}$), and Stem Number ($p = 2.615 \times 10^{-2}$). Figure 4 shows a heatmap of correlation coefficients between the 7-day centered moving averages of the water level or water temperature and the ground-truth parameters. Early July and September are shaded gray to indicate drainage periods. Regarding the daily average water level, positive correlations were observed for culm length, panicle number, and stem number, excluding overall length. Culm length showed strong correlations throughout most of the experimental period, except during drainage. Panicle number correlations were evident in mid-June, mid-July, and early August, while stem number correlations were observed during drainage. A statistically significant positive correlation (5% level) was confirmed between stem number and daily water level range during mid-season drainage. This aligns with agronomic knowledge that mid-season drainage promotes root development and suppresses ineffective tillering [23]. Stronger correlations were likely influenced by time lags of several hours to days in complete drainage across sampling points. Culm length showed strong positive correlations with the daily average water temperature around July 20 and throughout September. All parameters exhibited negative correlations with the daily water temperature range. For culm length, panicle number, and stem number, significant negative correlations (5% level) were observed in mid-June. These results reflect the general relationship that higher water temperatures promote plant growth, with culm length peaking from mid- to late July [24], [25], [26]. The negative correlation with daily temperature range in mid-June suggests that nighttime cooling increased variability, slowing growth.

3.2. Quartile-Based Analysis

Figure 6 shows the clustering results for a 3-m mesh size. The number of clusters was determined using the elbow and silhouette

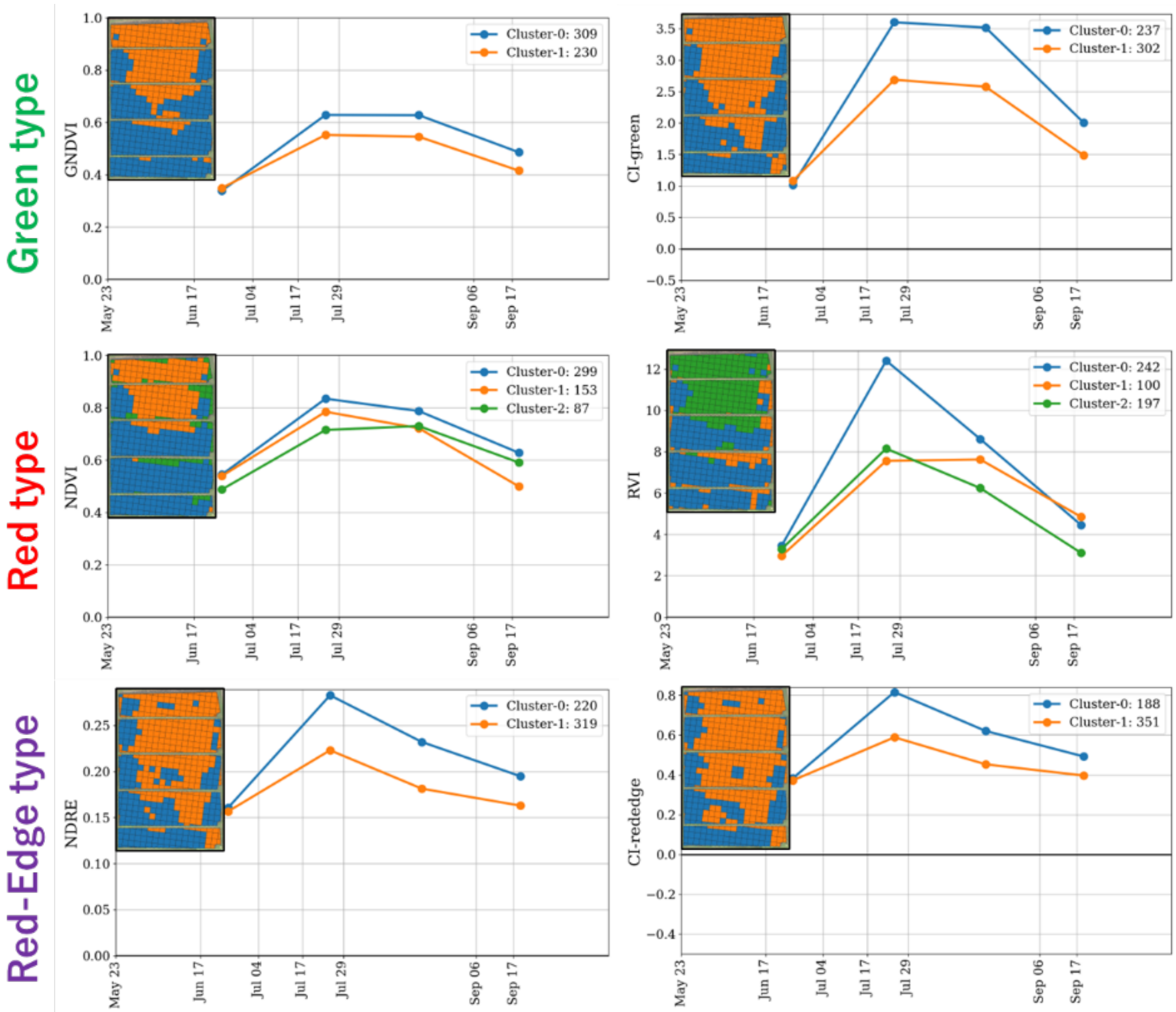

Figure 6: Clustering Results of Vegetation Indices for 3-m Square Mesh Size

scores. Using these methods, the number of clusters was set to two for the green type, three for the red type, and two for the red-edge type. On June 25, the value range was small for all the VIs, indicating limited spatial variability in crop growth. Another notable feature is that the VIs derived from the same spectral bands exhibited highly similar distribution patterns.

To visualize the relative growth differences within the field, the VI values for each mesh were divided into quartiles (25th-percentile intervals) and categorized from lowest to highest as Q1, Q2, Q3, and Q4. Figure 7 further visualizes the spatial distribution of quartile categories. The first four rows show quartile maps for each VI across survey dates, revealing little spatial variability in June and July. From August onward, distribution patterns resembling U-shaped and inverted triangular clusters became apparent. The fifth and sixth rows show the number of times each mesh was classified as Q1 or Q4 across all survey dates, while the seventh row shows the difference between Q4 and Q1 counts. These metrics provide an overview of growth conditions throughout the season. In particular, the Q4–Q1 difference effectively highlights areas with consistently favorable or poor growth. Although little spatial variation was observed until July, the distributions of Q1 and Q4 counts revealed growth differences corresponding to U-shaped and inverted triangular patterns.

Based on the cluster distribution maps, four characteristic spatial–temporal patterns were identified:

(1) Distributed in a U-shaped pattern within the site and associated with relatively favorable crop growth

(2) Distributed in an inverted triangular pattern within the site and associated with relatively poor crop growth.

(3) Located mainly in the southeastern part of the site, it is particularly evident in the red-edge-type indices. This suggests relatively higher stress within the U-shaped cluster.

(4) Represented by green meshes in NDVI and orange meshes in RVI, mainly appearing along the eastern edge of the site and near the ridges of Field-D. This cluster exhibited growth patterns similar to those of the inverted triangular cluster.

However, as reported in, [9], [10], and [21], the NDVI value of 0.7 at the heading stage (around the end of July) was not low, suggesting that the overall growth at the site was good.

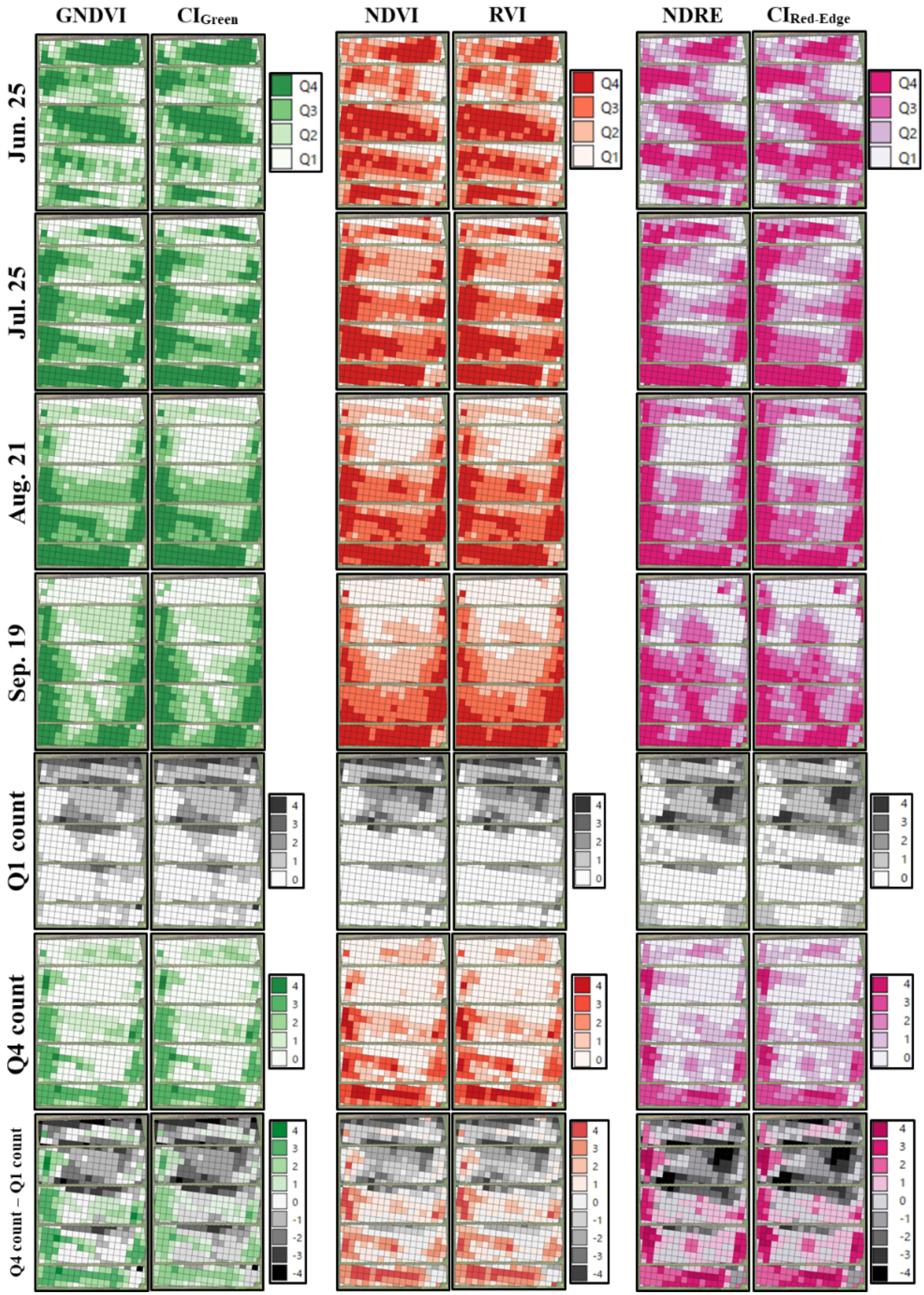

Figure 7: Spatial distribution maps of quartile-based categories (Q1–Q4) derived from vegetation index values for each UAV flight date (Jun. 25–Sep. 19), Q1 and Q4 classification counts across four UAV surveys (Q1 count and Q4 count), and the difference between Q4 and Q1 classification counts (Q4 count − Q1 count).

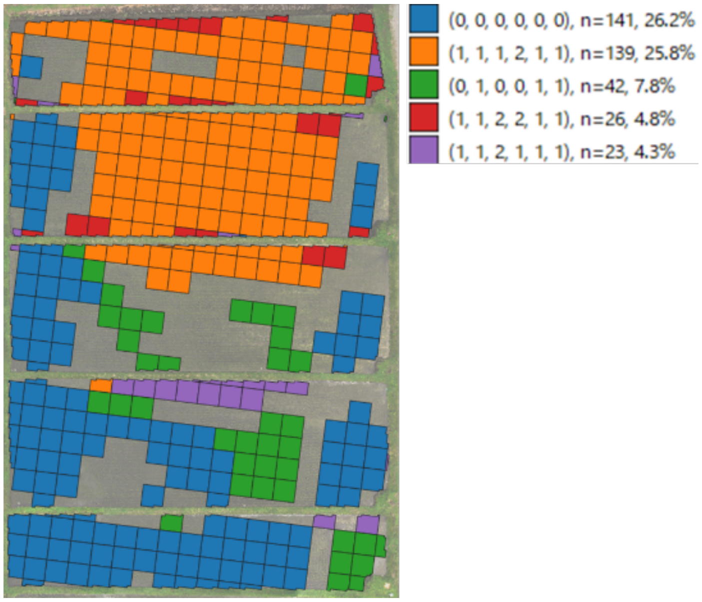

Figure 8: Top Five Most Frequent Combinations in The Grouping of Clustering Results in Figure 6. The legend indicates the combinations of VIs (GNDVI, CI_{Green}, NDVI, RVI, NDRE, $CI_{RedEdge}$), mesh counts, and their proportions.

4. Discussion

4.1. Investigation of Factors Underlying Crop Growth Temporal Patterns

Both the quartile-based and clustering-based analyses consistently identified U-shaped areas of vigorous growth and inverted triangular areas of poor growth. The field was considered susceptible to nutrient leaching because only basal fertilizer was applied before transplanting, with no additional fertilization during the growing season, and irrigation was managed using a continuous-flow system. Interviews with the farmer indicated that soil replacement was conducted in Fields A and B several years ago during nearby road expansion. Crop growth has reportedly been poorer in these fields since the civil work. This soil replacement may have altered soil organic matter and nutrient availability, contributing to the observed spatial variability in crop growth. However, this hypothesis could not be verified in the present study and requires confirmation through future soil analysis. Figure 8 shows the five most frequent groupings based on combinations of cluster IDs. Four of these combinations correspond to the patterns described in Section 3.2; blue represents (1), orange represents (2), green represents (3), and purple represents (4). The red combination corresponds to growth patterns similar to those of the orange and purple clusters. Although assessing and visualizing growth using individual VI cluster distribution maps is challenging, the combination distribution map provides a clearer overview, making it easier to interpret complex spatial growth patterns across the field.

Figure 10 shows a heatmap of correlation coefficients between VI values and ground-truth parameters. VI values were calculated as averages of the meshes overlapping each sample point. For the 3 m × 3 m grid, the green-type indices on June 25 showed a negative correlation between culm length and stem number. For the red-type indices, a negative correlation between overall length and stem number was observed on June 25, whereas a positive

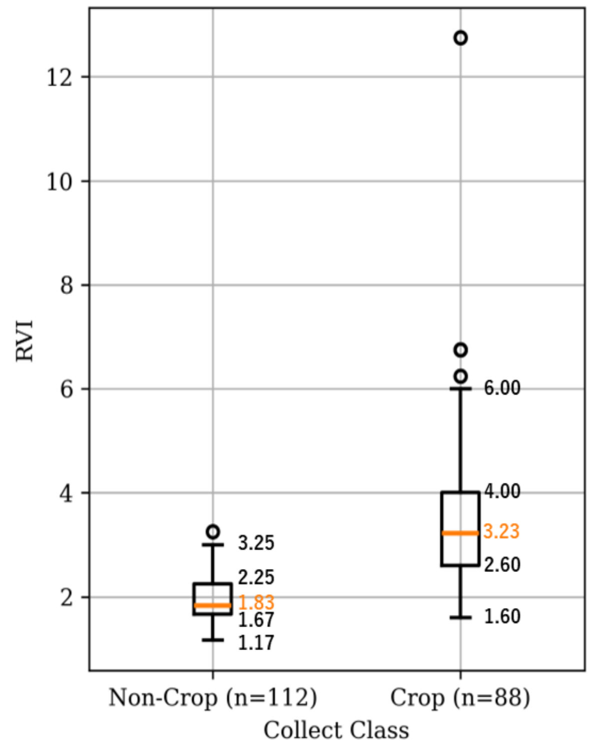

Figure 9: Boxplots of Random Points by Class

correlation between the stem number was observed on September 19. Figure 10 also compares results across three mesh sizes (1-m, 3-m, and 5-m squares), and the appropriate mesh size is discussed based on a comparison of these results. The correlations observed for the 3-m square grid generally showed similar trends to those of the 1-m and 5-m square meshes. For example, on June 25, the green-type indices showed a negative correlation between culm length and stem number, while the red-type indices showed a negative correlation with stem number. These results suggest that mesh sizes from 1 to 5 m yield comparable outcomes. For rice paddies, a larger grid size was considered acceptable, as UAV-based aerial photography is less affected by atmospheric conditions, and the rice paddies contain few objects other than rice. Previous studies have shown that mesh sizes smaller than 5 m are required to classify objects such as forest tree species or urban land use [27]. However, excessively small mesh sizes can introduce local noise and generate impractically large datasets. For example, using 2-cm squares, which corresponds to the same resolution as the aerial imagery used in this experiment, would result in approximately 15 million meshes, making clustering or GIS rendering computationally infeasible.

4.2. Addressing Low Vegetation Coverage in UAV Imagery

The Local Visual Method proposed in [9] performs crop–non-crop segmentation by determining VI thresholds for selected areas within a paddy field. Among the VIs listed in Table 1, MSAVI2 [28], RVI, and MSAVI2 achieved the best performance in crop–non-crop segmentation. To evaluate segmentation accuracy and usability, this study compared Local Visual, Otsu [29], [30], and clustering methods. RVI was selected for comparison because of its computational simplicity. To obtain the correct data, 40 points were randomly selected from each paddy field and manually classified as either crop or non-crop areas using QGIS. These data

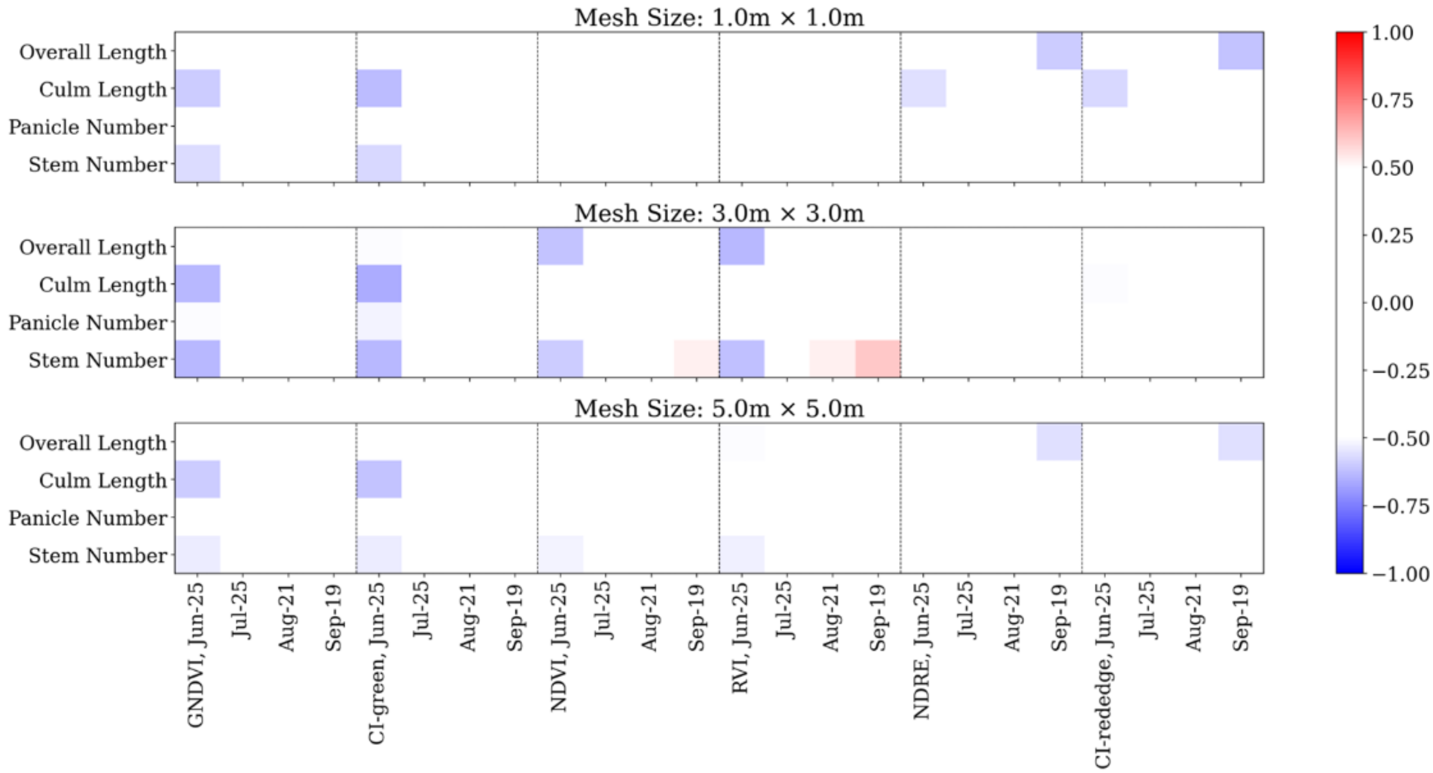

Figure 10: Correlations between Vegetation Indices and Survey Items. *: significant at the 5% level.

points are shown as "Random Points" in Figure 2. Figure 9 presents statistical plots of RVI values by class for the correct data. There were 200 correct data points, 88 in the crop class and 112 in the non-crop class. The mean ± standard deviation of the RVI was 3.60 ± 1.52 for the crop class and 1.96 ± 0.41 for the non-crop class. Welch's t-test confirmed a statistically significant difference between the two classes ($t = 9.88$, $p < 0.001$).

Table 2 summarizes the RVI thresholds determined by each method and the corresponding performance metrics based on confusion matrices. The thresholds are listed in ascending order as follows: Otsu, Local Visual, and Clustering. Otsu achieved the highest Accuracy, Recall, and F1-Score; Clustering achieved the highest Precision. Because the F1-Score was highest at a threshold of 2.272 in the brute-force approach, and the Otsu method produced a similar threshold, it achieved the best performance. The Otsu method requires minimal computational resources in comparison with other methods, can evaluate the entire image, and determines the threshold independently of the analyst. Therefore, this method is well-suited for removing non-crop areas. This study also applied the Otsu method for UAV imagery acquired in June to address the low vegetation coverage.

Table 2: Performance for Each Image Segmentation Method

Method (Threshold)	Otsu (2.53)	Local (2.90)	Clustering (3.70)	Best (2.27)
Accuracy	0.865	0.845	0.700	-
Precision	0.877	0.967	1.000	-
Recall	0.807	0.670	0.318	-
F1-Score	0.840	0.792	0.483	0.848

4.3. Development of an Automated Crop Diagnostic System

A previous study [9] presented a monitoring data analysis workflow and described the automated processing steps. The conventional workflow involves multiple software applications and more than 20 processing steps, making it highly complex. To reduce this complexity, most of the workflow was automated using a Python application programming interface (API). As an example, Figure 11 shows the interface for grid generation and calculations in QGIS. By selecting the orthophoto folder, mesh generation area, and mesh size, the reflectance values of each mesh in the orthophoto can be easily obtained. After generating and calculating small meshes, analysts manually label the area names (e.g., Field-A, ridge) for each mesh in a new column of the attribute table. Subsequently, the API generates meshes of arbitrary sizes for each labeled area by merging the original meshes. Mesh merging was also automated via another interface, where analysts input the number of merges. In the example shown in Figure 6, 0.25-m square meshes were generated, calculated, and labeled. A 3-m square mesh was then created by merging 12 meshes in both vertical and horizontal directions. This approach facilitates the generation of meshes of any size, even for non-rectangular fields, because field ridges and paddy fields do not mix within the mesh.

In the current version, manual field-area labeling is required only when analyzing the initial aerial survey data. In QGIS, all meshes within a field can be selected and labeled collectively as a polygon, making the process efficient and allowing labeling at the field level rather than at the mesh level. Nevertheless, full automation of this step is desirable. Future work will explore automated approaches using pre-cultivation aerial imagery, markers placed at field corners, and publicly available farmland parcel polygons.

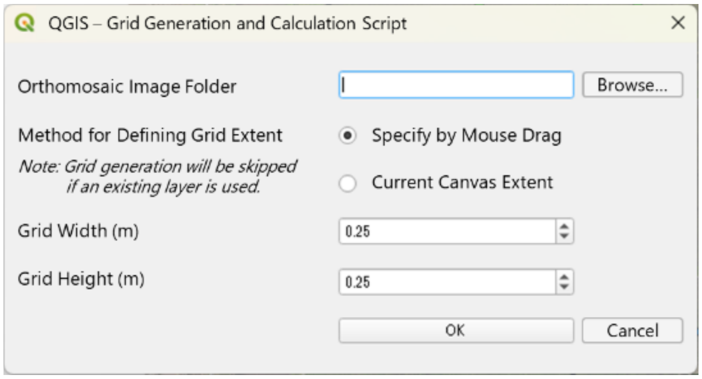

Figure 11: Input Interface for Grid Generation and Calculation in QGIS

5. Conclusion

Toward the development of a UAV-based crop growth diagnostic system, this study presented a quartile-based crop diagnostic method, mesh-size optimization, image calibration for low-vegetation-cover conditions, and systematization of the analytical workflow through a Python-based API. Correlation analysis between water sensor data from the experimental site and ground truth revealed strong negative correlations between low June temperatures and the water drainage period, with panicle and stem numbers. Quartile-based spatiotemporal analysis revealed spatial variability in crop growth, while the combined use of quartile- and clustering-based methods [9], [10], [21] provided deeper insights into the factors underlying the observed growth variability. Regarding mesh size optimization, no significant differences in the correlation trends between the VI values and ground truth were observed across mesh sizes ranging from 1 m × 1 m to 5 m × 5 m. Three image segmentation methods were compared to remove the non-crop areas. The results showed that Otsu's method achieved the best performance when evaluated using an F1-Score based on 200 randomly sampled points. An interface was developed for mapping optimization to enhance the automated analysis workflow described in [9]. It enables the creation and calculation of meshes of arbitrary sizes, even for non-rectangular fields, using attribute tables in QGIS.

Future research should focus on the development of diagnostic reports optimized for different crop species and environmental conditions. Farmers often face difficulty interpreting plots and visualizations without additional support, and the information required for crop management varies by species and cultivation objectives, for example, warnings related to high-temperature stress, disease occurrence, or soil moisture conditions. Although the analytical workflow itself may remain unchanged, diagnostic reports must be designed with sufficient flexibility and extensibility to accommodate different crop and management requirements. To achieve this, aerial and ground-truth data will be collected and matched across multiple locations and years to evaluate and generalize the diagnostic approach. In addition, feedback from farmers will be incorporated to identify practical diagnostic requirements and improve the applicability of the system. Moreover, while this study concentrated solely on crop diagnosis, the same procedures could be extended to surrounding areas. Certain weed species, particularly on sloped land such as vineyards, are intentionally preserved by farmers [31]. In Japan, farmland fragmentation and enclaves are major issues that increase production costs and contribute to farmland abandonment [32], [33]. Incorporating environmental monitoring into the diagnostic system would allow field characteristics to be evaluated more comprehensively, supporting farmland consolidation and broader agricultural land management initiatives.

Conflict of Interest

The authors declare no conflict of interest.

Acknowledgment

We thank Sustinere Co., Ltd. for their support during UAV flights. We are also grateful to The Bank of Iwate, Ltd., NTT EAST, Inc., and Japan Data Science Consortium Co., Ltd. for providing the experimental sites and assisting with ground-truth data collection. This manuscript was prepared with the assistance of ChatGPT (OpenAI) to improve the English language and language editing. The authors have reviewed, revised, and approved all AI-assisted texts and take full responsibility for the final content of the manuscript. We would also like to thank Editage (www.editage.jp) for the English language editing.

References

[1] Ministry of Agriculture, Forestry and Fisheries, "Census of Agriculture and Forestry in Japan," https://www.maff.go.jp/e/data/stat/index.html, 2026.

[2] Japan Meteorological Agency, "Global Warming Projection / TCC," https://www.data.jma.go.jp/tcc/tcc/products/gwp/gwp.html, 2026.

[3] Ministry of Agriculture, Forestry and Fisheries, "The Statistical Yearbook of MAFF," https://www.maff.go.jp/e/data/stat/nenji_index.htm, 2026.

[4] Ministry of Agriculture, Forestry and Fisheries, "Results of Agricultural Product Inspections of Rice," https://www.maff.go.jp/j/seisan/syoryu/kensa/kome/, 2026.

[5] V. Y. Chandrappa, B. Ray, N. Ashwatha, P. Shrestha, "Spatiotemporal modeling to predict soil moisture for sustainable smart irrigation," *Internet of Things*, **21**, 100671, 2023, doi:10.1016/j.iot.2022.100671.

[6] Ministry of Agriculture, Forestry and Fisheries, "Smart Agriculture," https://www.maff.go.jp/e/policies/tech_res/smaagri/robot.html, 2026.

[7] C. D. Villiers, Z. Mashaba-Munghemezulu, C. Munghemezulu, G. J. Chirima, S. Tesfamichael, "Assessing maize yield spatiotemporal variability using unmanned aerial vehicles and machine learning," *Geomatics*, **4**(3), 213–236, 2024, doi:10.3390/geomatics4030012.

[8] Y. Wang, S. Li, H. Cai, L. Deng, Y. Lin, "AGSPNet: A framework for parcel-scale crop fine-grained semantic change detection from UAV high-resolution imagery with agricultural geographic scene constraints," *Computers and Electronics in Agriculture*, **231**, 109973, 2025, doi:10.1016/j.compag.2025.109973.

[9] T. Ito, K. Minamino, "Analysis Workflow Improvement and Integrated Diagnosis of Vegetation Indices Toward an Unmanned Aerial Vehicle-Based Field Diagnostic System," in *The 10th International Conference on Machine Learning and Soft Computing (ICMLSC 2026)*, 2026.

[10] T. Ito, K. Minamino, S. Umeki, "Visualization of the effect of additional fertilization on paddy rice by time-series analysis of vegetation indices using UAV and minimizing the number of monitoring days for its workload reduction," *Advances in Science, Technology and Engineering Systems Journal*, **9**(3), 29–40, 2024, doi:10.25046/aj090303.

[11] R. de Souza, C. Buchhart, K. Heil, J. Plass, F. M. Padilla, U. Schmidhalter, "Effect of time of day and sky conditions on different vegetation indices calculated from active and passive sensors and images taken from UAV," *Remote Sensing*, **13**(9), 1691, 2021, doi:10.3390/rs13091691.

[12] M. Louhaichi, M. M. Borman, D. E. Johnson, "Spatially located platform and aerial photography for documentation of grazing impacts on wheat,"

Geocarto International, **16**(1), 65–70, 2001, doi:10.1080/10106040108542184.

[13] A. A. Gitelson, A. Viña, T. J. Arkebauer, D. C. Rundquist, G. Keydan, B. Leavitt, "Remote estimation of leaf area index and green leaf biomass in maize canopies," *Geophysical Research Letters*, **30**(5), 1248, 2003, doi:10.1029/2002GL016450.

[14] J. W. Rouse, R. H. Haas, J. A. Schell, D. W. Deering, "Monitoring vegetation systems in the Great Plains with ERTS," in *Third Earth Resources Technolofy Satellite-1 Symposium*, Washington, DC, USA, 1974.

[15] C. F. Jordan, "Derivation of leaf-area index from quality of light on the forest floor," *Ecology*, **50**(4), 663–666, 1969, doi:10.2307/1936256.

[16] E. M. Barnes, T. R. Clarke, S. E. Richards, P. D. Colaizzi, J. Haberland, M. Kostzewski, P. Waller, C. Choi, E. Riley, T. Thompson, R. J. Lascano, H. Li, M. S. Moran, "Coincident detection of crop water stress, nitrogen status and canopy density using ground-based multispectral data," in *Proceedings of the 5th International Conference on Precision Agriculture*, Bloomington, Minnesota, USA, 2000.

[17] A. A. Gitelson, Y. Gritz, M. N. Merzlyak, "Relationships between leaf chlorophyll content and spectral reflectance and algorithms for non-destructive chlorophyll assessment in higher plant leaves," *Journal of Plant Physiology*, **160**(3), 271–292, 2003, doi:10.1078/0176-1617-00887.

[18] C. Hongo, T. Kobayashi, Y. Arita, "The response of water status in tree seedlings through spectral reflectance," *Journal of the Japan Society of Photogrammetry and Remote Sensing*, **37**(4), 43–50, 1998, doi:10.4287/jsprs.37.4_43.

[19] J. Xue, B. Su, "Significant remote sensing vegetation indices: A review of developments and applications," *Journal of Sensors*, **2017**(1), 1353691, 2017, doi:10.1155/2017/1353691.

[20] S. Khanal, K. KC, J. P. Fulton, S. Shearer, E. Ozkan, "Remote sensing in agriculture—Accomplishments, limitations, and opportunities," *Remote Sensing*, **12**(22), 3783, 2020, doi:10.3390/rs12223783.

[21] T. Ito, K. Minamino, S. Umeki, "Time-Series Clustering Analysis of Vegetation Indices Obtained from UAV to Visualize Fertilization Effect and High Temperature Influence," in *The 6th International Symposium on Advanced Technologies and Applications in the Internet of Things (ATAIT 2024)*, 83–92, 2024.

[22] R. Tavenard, J. Faouzi, G. Vandewiele, F. Divo, G. Androz, C. Holtz, M. Payne, R. Yurchak, M. Rußwurm, K. Kolar, and E. Woods, "Tslearn, A Machine Learning Toolkit for Time Series Data," *Journal of Machine Learning Research*, **21**(118), pp. 1–6, 2020.

[23] Q. Wu, Y. He, Z. Qi, Q. Jiang, "Drainage in paddy systems maintains rice yield and reduces total greenhouse gas emissions on the global scale," *Journal of Cleaner Production*, **370**, 133515, 2022, doi:10.1016/j.jclepro.2022.133515.

[24] H. Shimono, T. Hasegawa, K. Iwama, "Response of growth and grain yield in paddy rice to cool water at different growth stages," *Field Crops Research*, **73**(2–3), 67–79, 2002, doi:10.1016/S0378-4290(01)00184-8.

[25] T. Kuwagata, T. Hamasaki, T. Watanabe, "Modeling water temperature in a rice paddy for agro-environmental research," *Agricultural and Forest Meteorology*, **148**(11), 1754–1766, 2008, doi:10.1016/j.agrformet.2008.06.011.

[26] S. Li, H. Jiang, J. Wang, Y. Wang, S. Pan, H. Tian, M. Duan, S. Wang, X. Tang, Z. Mo, "Responses of plant growth, physiological, gas exchange parameters of super and non-super rice to rhizosphere temperature at the tillering stage," *Scientific Reports*, **9**, 10618, 2019, doi:10.1038/s41598-019-47031-9.

[27] A. M. Lechner, A. Stein, S. D. Jones, J. G. Ferwerda, "Remote sensing of small and linear features: Quantifying the effects of patch size and length, grid position and detectability on land cover mapping," *Remote Sensing of Environment*, **113**(10), 2194–2204, 2009, doi:10.1016/j.rse.2009.06.002.

[28] J. M. Chen, "Evaluation of vegetation indices and a modified simple ratio for boreal applications," *Canadian Journal of Remote Sensing*, **22**(3), 229–242, 1996, doi:10.1080/07038992.1996.10855178.

[29] N. Otsu, "A threshold selection method from gray-level histograms," *IEEE Transactions on Systems, Man, and Cybernetics*, **9**(1), 62–66, 1979, doi:10.1109/TSMC.1979.4310076.

[30] S. L. Bangare, A. Dubal, P. S. Bangare, S. T. Patil, "Reviewing Otsu's method for image thresholding," *International Journal of Applied Engineering Research*, **10**(9), 21777–21783, 2015.

[31] S. Iriuda, K. Minamino, "Soil diagnosis and weed species identification using drone with multispectral cameras and machine learning," *Journal of the Japan Society of Infrared Science and Technology*, **35**(1), 16–24, 2025.

[32] K. Kawasaki, "The costs and benefits of land fragmentation of rice farms in Japan," *Australian Journal of Agricultural and Resource Economics*, **54**(4), 509–526, 2010, doi:10.1111/j.1467-8489.2010.00509.x.

[33] G. Su, H. Okahashi, L. Chen, "Spatial pattern of farmland abandonment in Japan: Identification and determinants," *Sustainability*, **10**(10), 3676, 2018, doi:10.3390/su10103676.